

IXGS—Intraoperative 3D Reconstruction from Sparse, Arbitrarily Posed Real X-rays

Sascha Jecklin^{1,*}, Aidana Massalimova¹, Ruyi Zha³, Lilian Calvet¹, Christoph J. Laux², Mazda Farshad², and Philipp Frnstahl¹

¹Research in Orthopedic Computer Science, Balgrist University Hospital, Zurich, 8008, Switzerland

²Department of Orthopedics, Balgrist University Hospital, University of Zurich, Zurich, 8008, Switzerland

³The Australian National University, Canberra, ACT 2601, Australia

*sascha.jecklin@balgrist.ch

ABSTRACT

Spine surgery is a high-risk intervention demanding precise execution, often supported by image-based navigation systems. Recently, supervised learning approaches have gained attention for reconstructing 3D spinal anatomy from sparse fluoroscopic data, significantly reducing reliance on radiation-intensive 3D imaging systems. However, these methods typically require large amounts of annotated training data and may struggle to generalize across varying patient anatomies or imaging conditions. Instance-learning approaches like Gaussian splatting could offer an alternative by avoiding extensive annotation requirements. While Gaussian splatting has shown promise for novel view synthesis, its application to sparse, arbitrarily posed real intraoperative X-rays has remained largely unexplored.

This work addresses this limitation by extending the R^2 -Gaussian splatting framework to reconstruct anatomically consistent 3D volumes under these challenging conditions. We introduce an anatomy-guided radiographic standardization step using style transfer, improving visual consistency across views, and enhancing reconstruction quality. Notably, our framework requires no pretraining, making it inherently adaptable to new patients and anatomies.

We evaluated our approach using an *ex-vivo* dataset. Expert surgical evaluation confirmed the clinical utility of the 3D reconstructions for navigation, especially when using 20 to 30 views, and highlighted the standardization’s benefit for anatomical clarity. Benchmarking via quantitative 2D metrics (PSNR/SSIM) confirmed performance trade-offs compared to idealized settings, but also validated the improvement gained from standardization over raw inputs.

This work demonstrates the feasibility of instance-based volumetric reconstruction from arbitrary sparse-view X-rays, advancing intraoperative 3D imaging for surgical navigation. Code and data to reproduce our results is made available at <https://github.com/MrMonk3y/IXGS>.

Introduction

Studies have demonstrated that surgical navigation can contribute to an improved patient outcome, reduce complications, shorten operating time, and lower revision rates^{1,2}. Clinically established navigation systems primarily rely on either preoperative imaging registered to the patient’s anatomy during surgery or directly utilize intraoperative 3D imaging for guidance.

Widely used registration-based approaches utilize point-, contour-, or intensity-based registration, where preoperative computed tomography (CT) data is registered to the patient’s anatomy during surgery^{3–5}. Deep learning-based methods have been proposed to improve registration accuracy and robustness^{6,7}. However, registration remains a highly ill-posed problem, making the process susceptible to data ambiguity, user-dependent variability, and anatomical changes^{8,9}.

Intraoperative 3D imaging devices such as cone-beam computed tomography (CBCT) enable high-resolution intraoperative 3D reconstructions for spinal procedures and eliminates the need for registration. However, this advantage comes at the cost of increased radiation exposure. CBCT typically requires between 180 and 1024 projections to reconstruct a 3D volume¹⁰. The patient radiation dose for spinal procedures using CBCT can increase by 2.8 to 9.96 times compared to conventional 2D fluoroscopy^{11–13}. Beyond radiation risks, CBCT also has technical limitations such as a restricted field of view, more elaborate draping requirements, and longer acquisition times compared to conventional 2D fluoroscopy^{1,11,14,15}. Reducing intraoperative radiation while maintaining high-quality 3D reconstructions is therefore a key objective.

Previous research has focused on preserving the benefits of high-quality (CBCT-like) intraoperative 3D reconstruction while reducing radiation exposure, particularly in spinal procedures. In our prior work, X23D, we demonstrated that a neural network can accurately reconstruct a 3D volume of the lumbar spine from only four X-rays using a neural network, achieving high accuracy with low radiation exposure^{16,17}. X23D integrates prior anatomical knowledge through end-to-end training on a large, curated dataset. However, this approach limits its scalability, particularly when accommodating the full spectrum of

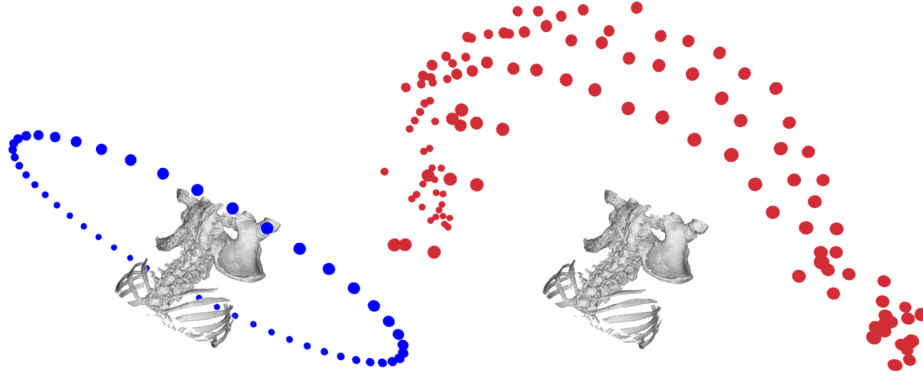


Figure 1. Comparison between conventional circular acquisition paths, typical for CBCT/CT imaging or idealized synthetic DRR generation (left), and the irregular, arbitrary acquisition poses representative of real intraoperative settings (right).

anatomical variations, pathological conditions, and implant types encountered in the operating room.

Neural scene representation techniques overcome these limitations, as they are capable of synthesizing high-quality 3D representations from sparse 2D data without requiring pretraining^{18–20}. Compared to our previous work, X23D, their architecture allows for processing larger images on similar hardware, accommodating larger scenes without losing resolution.

Although these representation techniques show promise in medical imaging, such as X-rays and ultrasound, achieving accurate 3D density reconstruction with clinically acceptable quality remains challenging, especially under intraoperative conditions. For Gaussian splatting specifically, the R^2 -Gaussian approach¹⁸ introduced a rectification strategy for an integration bias that previously limited volumetric accuracy. On realistic anatomy, the method was evaluated only through synthetic, digitally reconstructed radiographs (DRRs), generated from a human torso CT. At the same time, validation on real X-rays was limited to simple, small objects such as pinecones and seashells, lacking the complexity and variability present in real intraoperative settings. Both synthetic and real data experiments relied on the simplification of circular acquisition trajectories. In surgical scenarios, however, methods must perform robustly with arbitrarily posed X-rays, as commonly encountered in intraoperative imaging (illustrated in Figure 1). Imaging parameters such as kVp and mAs — and therefore image contrast and brightness — can vary noticeably from acquisition to acquisition. While R^2 -Gaussian¹⁸ can generate reasonable novel views when trained on real X-rays, we observed (and literature confirms^{21,22}) that the quality of the reconstructed 3D volume is noticeably degraded under such real-world conditions.

In this work, we extend R^2 -Gaussian splatting¹⁸ to handle arbitrary poses and investigate its feasibility in generating 3D visualizations for surgical navigation from a sparse set of real, intraoperative 2D X-ray images. Real imaging conditions can vary greatly, and the images are often degraded by noise and other artifacts. To address this challenge, we introduce an anatomy-guided radiographic standardization step as a crucial preprocessing component. This step, implemented via a style transfer network²³ trained on our paired *ex-vivo* dataset¹⁷, maps real X-rays into a standardized domain, enhancing consistency and emphasizing bone structures to allow the subsequent Gaussian splatting optimization to focus more effectively. Following standardization, these processed images and their corresponding poses are used to optimize the 3D Gaussian representation. Finally, the optimized splats are converted into a volumetric density map, which undergoes thresholding and cropping before visualization via direct rendering or clinical slice views.

Building upon this approach, our work explores the following two hypotheses: First, can Gaussian splatting generate 3D visualizations from sparse 2D X-rays that are deemed sufficiently accurate by experts for surgical navigation? Second, what is the minimum number of input X-rays required to produce a visualization of sufficient accuracy? To answer these questions, we first evaluated the quality of the visualization via expert ratings from an experienced surgeon, assessing whether the visualizations meet the requirements for intraoperative navigation. Additionally, we assessed the quality using the established 2D image similarity metrics PSNR and SSIM, allowing direct comparison to existing methods that rely on synthetic and circularly captured data.

A main contribution of this work is the proposed IXGS framework. This framework extends the R^2 -Gaussian splatting approach to process arbitrary-posed real X-rays, demonstrating feasibility beyond previously evaluated circular acquisition paths. This was significantly aided by improving 3D volume consistency through a novel preprocessing step that emphasizes bony features using style transfer. Furthermore, the study provides guidelines regarding the number of views required to generate clinically acceptable reconstructions using this approach.

We will release our code for 3D reconstruction from arbitrary X-rays, with a small dataset for testing, on <https://github.com/MrMonk3y/IXGS>.

Related Work

Related work is reviewed in the following subsections, covering sparse-view 3D reconstruction in Section , Gaussian splatting and neural radiance fields, especially in medical applications in Section , and preprocessing methods tackling the isolation of relevant anatomical regions in Section .

Sparse-View 3D Reconstruction

In contrast to CT and CBCT, which generate high-quality 3D reconstructions from densely sampled sweeps, sparse-view approaches aim to achieve similar results with fewer projections. Several prior works have proposed methods to reconstruct 3D volumes from sparse X-ray views, each differing in anatomical focus and reconstruction quality. Kasten et al.²⁴ presented a U-net architecture that uses only two orthogonal X-rays of the knee anatomy, achieving a 90% F1 score. Their approach primarily relied on synthetic training data, using DRRs generated from CT scans. To apply the trained model to real X-rays, they proposed an unpaired style transfer network to adapt real intraoperative X-rays into the appearance domain of the synthetic training data. Shiode et al.²⁵ proposed a similar approach for the forearm, using a single X-ray image. They trained a Pix2Pix network on a small paired dataset of DRRs created through intensity-based registration of real X-rays. Although effective for specific anatomies, these methods rely on preoperative, diagnostic X-rays with near-orthogonal views, which are difficult to obtain consistently in realistic intraoperative settings. Another limitation is that end-to-end trained methods learn a priori knowledge, struggling to reconstruct patient-specific variations or pathologies.

²⁶ presented X-CTRSNet, which reconstructed cervical vertebrae from two orthogonal views, achieving an 80.4% F1 score. Their method handles real X-rays but requires standardized, well-aligned orthogonal projections and is limited to a small reconstruction volume of 128^3 voxels. In our own X23D approach^{16,17}, we adapt a learnt stereo machine²⁷ to reconstruct the lumbar spine from four arbitrarily posed intraoperative X-rays, reaching 84% F1 score on real data. This two-stage method combined a style transfer network trained to bridge the synthetic-real domain gap, followed by a reconstruction network extensively trained on synthetic data. X23D showed promising accuracy and performance²⁸.

Overall, existing sparse-view approaches demand substantial pretraining on anatomical datasets, making them prone to overfitting and limited in handling unseen pathologies or new anatomies. They also rely on voxelized outputs, which impose a trade-off between reconstruction volume size and resolution. In practice, capturing an entire bone (e.g., a femur) requires larger volumes, which can compromise the resolution of fine structural details like fracture lines. Finally, current sparse-view reconstructions lack calibrated Hounsfield units, resulting in density values that may not match those seen in traditional CT.

Gaussian Splatting and Neural Radiance Fields

Recent approaches for generating 3D scenes from images without extensive pretraining include neural radiance fields (NeRF)²⁹ and Gaussian splatting³⁰. While NeRF typically uses implicit neural networks to represent scene density and color as a continuous field, Gaussian splatting uses an explicit representation. This representation displays the scene as a collection of 3D Gaussian primitives defined by properties such as position, covariance, opacity, and appearance coefficients. This representation allows Gaussian splatting to offer memory and computational benefits compared to NeRF-based approaches. Although both approaches were originally developed for novel view synthesis, their volumetric representations can also be converted into meshes for surface reconstruction³¹. Both techniques and synthetic X-ray-based reconstructions^{32–37}.

The authors of SAX-NeRF³⁸ were among the first to adapt NeRF for X-ray visualization by encoding density values instead of color and opacity. They introduced a line segment-based transformer and a ray sampling strategy to extract contextual and geometric information from the 2D projections. Although SAX-NeRF improved density reconstruction, it requires more than 13 hours to train on just 25 images¹⁸.

R^2 -Gaussian¹⁸ built on Gaussian splatting to reduce training time to under 3 minutes for 25 images. R^2 -Gaussian also introduced an integration bias rectification technique that significantly enhanced volumetric reconstruction quality. The method was tested on 25, 50, and 75 synthetic torso DRRs generated from circular sweeps and on real X-rays of relatively simple objects (e.g., walnuts, pine cones) from the FIPS X-ray Tomographic dataset³⁹.

When applied to real intraoperative X-rays, the quality of the reconstructed 3D volume degraded substantially in our experiments, due to more complex anatomy and larger imaging variations. Literature confirmed our observations. The complexity of the underlying topology and variations in imaging conditions can significantly impact the quality of the 3D volume. Previous work^{21,22} has shown that factors like brightness variations, noise, and artifacts pose severe challenges to 3D Gaussian splatting.

To address these challenges associated with real X-rays, we developed the IXGS framework. This approach extends R^2 -Gaussian splatting to process arbitrarily posed images and introduces an anatomy-guided radiographic standardization step.

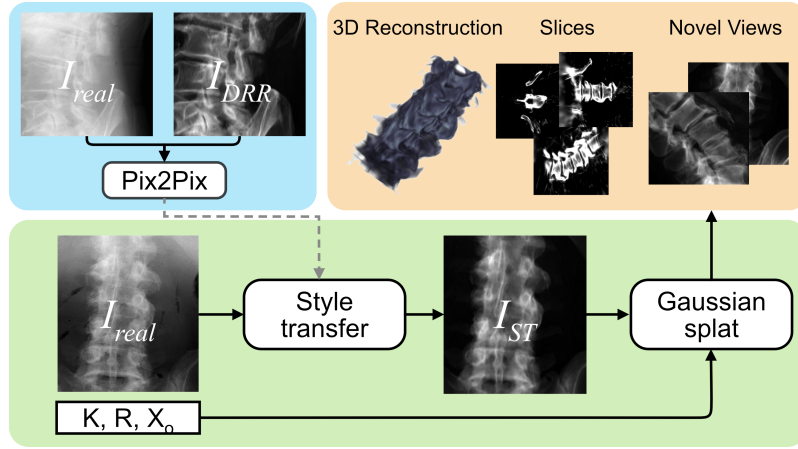


Figure 2. Pipeline Overview. The training of Pix2Pix (blue) uses paired real X-rays (I_{real}) and synthetic DRRs (I_{DRR}) to learn style transfer. During inference (green), real X-rays with calibration information are converted to style-transferred images (I_{ST}). These images, along with their poses, are passed to the Gaussian splatting network, which outputs 3D reconstructions. The resulting volume can be visualized as slices or rendered from arbitrary viewpoints (orange).

Preprocessing Methods

Several preprocessing concepts have been proposed to spatially isolate relevant anatomical regions and enhance their visualization quality. These techniques are particularly useful when working with real intraoperative X-rays, where noise, artifacts, and overlying or adjacent tissues complicate reconstruction.

One possible approach is segmentation, where only relevant structures such as bones are preserved, while soft tissues and background areas are masked. This simplifies the reconstruction task by guiding the network on the structures of interest. State-of-the-art segmentation networks tailored to bone and spine anatomy have shown promising results^{40,41}. However, training segmentation networks requires extensive manual annotation to create labeled datasets, which is costly and time-consuming, especially for intraoperative imaging. Recently, pre-trained vision transformer models such as DINOv2⁴² and SAM⁴³ have demonstrated strong performance in object segmentation, even without explicit annotations. To further improve segmentation performance for medical data, specialized adaptations such as Medical SAM have been developed⁴⁴. Despite these advances, segmentation methods still struggle with low contrast, overlapping structures, and anatomical variability, especially in intraoperative X-rays, limiting their robustness in real surgical environments⁴⁵.

An alternative is localization, which identifies the approximate region of interest and crops the X-ray accordingly, similar to collimation in traditional radiography. Localization requires less precision than full segmentation and can be performed using lightweight neural networks. Beyond general-purpose localization networks⁴⁶, approaches trained and tailored to medical imaging applications have been proposed^{47,48}. In our previous work, we used ground truth X-ray poses and 3D CT segmentation to project individual lumbar vertebrae into the X-ray images. These projections were then used to train a YOLOv7 network⁴⁹ to localize and crop the corresponding vertebrae in real X-rays¹⁷.

In addition to spatial isolation, appearance-based preprocessing techniques such as style transfer can enhance the visibility of critical structures and normalize image appearance across different views. Style transfer has been widely used to change the appearance in certain aspects, particularly in sparse-view reconstruction pipelines with synthetic training data^{17,24,25}. Paired style transfer methods, such as Pix2Pix²³, leverage these paired synthetic-real datasets to train a direct mapping between domains. Unpaired methods, such as CycleGAN⁵⁰, learn this mapping without requiring exact correspondence, making them more flexible when paired data is unavailable.

Methods

This section details our methodology for the high-quality 3D reconstruction of the spine anatomy from sparse and arbitrarily posed intraoperative X-rays. An overview of the pipeline is shown in Figure 2. The process begins with acquiring and calibrating *ex-vivo* CT and X-ray data to generate a paired real-synthetic dataset for training and validation (Sections). We then employ anatomy-guided radiographic standardization, using a Pix2Pix model²³ trained on this paired data, to transform real X-rays into a standardized domain (Section). Subsequently, geometric preprocessing, including image cropping and volume normalization is applied to ensure compatibility with the reconstruction network (Section). Following this, volumetric 3D reconstruction is performed on these prepared views using our IXGS framework (Section). The performance of this pipeline is

then evaluated through experiments detailed in Section , which include a qualitative assessment of 3D clinical usability by an expert surgeon and quantitative benchmarking of 2D view synthesis quality using standard metrics against baseline conditions.

Dataset

This study utilizes a paired dataset comprising spatially aligned real X-ray images \mathbf{I}_{real} and corresponding synthetic DRRs \mathbf{I}_{DRR} generated from CT scans. This specialized dataset served two critical purposes within our pipeline: first, it provided the necessary aligned image pairs for training the Pix2Pix network used in the anatomy-guided radiographic standardization step (Section). Second, it served as ground truth data and a defined target domain for benchmarking reconstruction performance and evaluating the effectiveness of the standardization process (Section). The detailed construction of this dataset, including calibration and pairing, has been described in detail in our previous work¹⁷. The data collection process can be summarized as follows.

We constructed a data collection pipeline to acquire such a paired *ex-vivo* dataset consisting of real \mathbf{I}_{real} and \mathbf{I}_{DRR} images captured from the same arbitrary viewpoints, along with their corresponding pose information. The study was conducted according to the guidelines of the Declaration of Helsinki and approved by the local ethical committee (KEK Zurich BASEC No. 2021-01083). The CT data was obtained using a SOMATOM Edge Plus system (Siemens Healthcare, Erlangen, Germany), providing 0.75 mm slice thickness and 0.5 mm \times 0.5 mm in-plane resolution. Subsequently, segmentations of the L1 to L5 vertebrae within these CT volumes were generated by trained specialists employing Mimics software (Version 25.0, Materialise NV, Leuven, Belgium). Although the reconstructed 3D volumes in this work do not exhibit clear surface boundaries suitable for direct mesh extraction, these segmentations served as ground truth references during qualitative evaluation.

X-rays were acquired from anterior-posterior (AP), lateral, and oblique views using a clinical-grade mobile C-arm (Cios Spin®, Siemens Healthineers, Erlangen, Germany). The C-arm was rotated in 3° increments over a transverse orbit of $\pm 102^\circ$ and tilted in 3° increments over a sagittal range of $\pm 25^\circ$. Additional lateral views were captured with 5° sagittal tilts over a range of $\pm 15^\circ$. The X-ray beam was centered on the L3 vertebra to ensure full coverage of the lumbar spine.

To achieve accurate pose information, 14 stainless steel spherical fiducials were inserted into the soft tissue surrounding the spinal column from L1 to L5. A post-fiducial placement CT scan was acquired to determine the 3D positions of the fiducials, which were identified through thresholding and 3D connected component analysis.

The calibration process involved detecting fiducial projections in the X-rays using a circular Hough transform⁵¹, followed by user verification if necessary. Initial pose estimates were obtained using the direct linear transform (DLT) algorithm⁵², refined with a RANSAC-based process to minimize reprojection error. Once optimal correspondences were established, the final camera matrix \mathbf{P} was estimated using all fiducials. This matrix was then decomposed into intrinsic parameters \mathbf{K} , the rotation matrix \mathbf{R} , and the camera origin \mathbf{X}_o . To preserve realism in the dataset, fiducial projections were subsequently inpainted from the X-rays.

Following this, for each real X-ray \mathbf{I}_{real} , a synthetic \mathbf{I}_{DRR} was generated from the corresponding CT scan and calibration information. The transformation from world space to C-arm space is defined by the matrix

$$\mathbf{T} = \begin{bmatrix} \mathbf{R} & \mathbf{X}_o \\ \mathbf{0}^\top & 1 \end{bmatrix}, \quad (1)$$

which incorporates the extrinsic camera parameters. The DRR at pixel p is computed by:

$$\mathbf{I}_{\text{DRR}}(p) = \int A \left(\mathbf{T}^{-1} L(p, s) \right) \mathbf{1} \left(A \left(\mathbf{T}^{-1} L(p, s) \right) > t \right) ds \quad (2)$$

where A denotes the CT attenuation values, $L(p, s)$ is the ray passing through pixel p parameterized by depth s , and $\mathbf{1}(\cdot)$ is an indicator function returning 1 if the attenuation exceeds a threshold t . For this study, we set $t = 0$ Hounsfield units to isolate bone structures.

This study utilized six *ex-vivo* human specimens selected from the original dataset created in¹⁷. The selection ensured that each specimen had at least 50 X-rays available for training, along with a sufficient number of images for testing. For each *ex-vivo* specimen, 50 X-rays were randomly sampled to form the training set, encompassing a diverse range of views including anterior-posterior, lateral, oblique, and off-axis shots. This resulted in a total of 300 training images. The remaining X-rays were reserved as dedicated test sets for each specimen, resulting in a combined test set of 233 images. Notably, the same test set was used consistently across all experiments, regardless of the number of training views.

Anatomy-guided Radiographic Standardization

To ensure consistent input quality and emphasize key anatomical structures, we applied an anatomy-guided radiographic standardization step before feeding the images to the Gaussian splatting network. This preprocessing step aims to isolate the

region of interest, enhance bone structures, and reduce variability in appearance caused by, e.g., noise and artifacts present in real X-rays. By mapping real X-ray images to a standardized synthetic domain, we improve the robustness of the subsequent volumetric reconstruction process.

The paired real X-ray images \mathbf{I}_{real} and synthetic DRRs \mathbf{I}_{DRR} were used to train a Pix2Pix model²³. The objective of the generative adversarial network (GAN) is to map \mathbf{I}_{real} to the domain of \mathbf{I}_{DRR} , emphasizing bone structures and ensuring a consistent visual appearance across all views. This standardization process is critical for enabling the Gaussian splatting network to effectively focus on relevant anatomical features necessary for accurate 3D reconstruction.

The GAN consists of a generator G and a discriminator D . These are optimized using a combination of adversarial loss $\mathcal{L}_{\text{cGAN}}$ and L1 loss \mathcal{L}_{L1} to improve image quality and reduce blurring, defined as follows:

$$\mathcal{L}_{\text{cGAN}}(G, D) = \mathbb{E}_{\mathbf{I}_{\text{real}}, \mathbf{I}_{\text{DRR}}} [\log D(\mathbf{I}_{\text{real}}, \mathbf{I}_{\text{DRR}})] + \mathbb{E}_{\mathbf{I}_{\text{real}}, z} [\log(1 - D(\mathbf{I}_{\text{real}}, G(\mathbf{I}_{\text{real}}, z)))] \quad (3)$$

$$\mathcal{L}_{\text{L1}}(G) = \mathbb{E}_{\mathbf{I}_{\text{real}}, \mathbf{I}_{\text{DRR}}, z} [\|\mathbf{I}_{\text{DRR}} - G(\mathbf{I}_{\text{real}}, z)\|_1] \quad (4)$$

$$G^* = \arg \min_G \max_D \mathcal{L}_{\text{cGAN}}(G, D) + \lambda \mathcal{L}_{\text{L1}}(G) \quad (5)$$

Here, the variable z denotes random noise input to the generator G , typically introduced via dropout, allowing for stochasticity in the generated output $G(\mathbf{I}_{\text{real}}, z)$.

To prevent information leakage, a separate Pix2Pix model was trained for each *ex-vivo* specimen, ensuring that each test specimen remained completely excluded from its corresponding training set. After training, the generator G was used to style-transfer \mathbf{I}_{real} to the synthetic domain, producing $\mathbf{I}_{\text{ST}} = G(\mathbf{I}_{\text{real}})$.

Preprocessing: Cropping and Volume Normalization

After anatomy-guided radiographic standardization, additional preprocessing steps were applied to all synthetic and real images to ensure compatibility with the Gaussian splatting network.

Due to slight mechanical deflection of the C-arm under gravitational load, the principal point (c_x, c_y) derived from the intrinsic matrix \mathbf{K} during calibration is often not centered in the image. Since Gaussian splatting assumes a centered principal point; we cropped the images around (c_x, c_y) to ensure alignment within a fixed resolution of 512×512 pixels.

Furthermore, the 3D volume to be reconstructed via Gaussian splatting was normalized to fit within the spatial range $[-1, 1]^3$. This normalization is required by Gaussian splatting frameworks to ensure consistent handling of spatial coordinates during training and inference.

3D Reconstruction via Gaussian Splatting

Our IXGS approach builds upon the R^2 -Gaussian splatting framework introduced by Zha et al.¹⁸. The method represents the target anatomical structure by a collection of learnable Gaussian kernels $\mathbb{G}^3 = \{G_j^3\}_{j=1, \dots, M}$. Each Gaussian kernel G_j^3 describes a local density distribution in 3D space:

$$G_j^3(\mathbf{x}) = \rho_j \exp\left(-\frac{1}{2}(\mathbf{x} - \mathbf{p}_j)^\top \Sigma_j^{-1}(\mathbf{x} - \mathbf{p}_j)\right), \quad (6)$$

where $\mathbf{x} \in \mathbb{R}^3$ is a point in world coordinates, $\rho_j \in \mathbb{R}$ represents the central density, $\mathbf{p}_j \in \mathbb{R}^3$ the position of the kernel, and $\Sigma_j \in \mathbb{R}^{3 \times 3}$ its covariance matrix. Unlike standard 3D Gaussian splatting methods, the¹⁸ approach omits view-dependent color information since X-ray imaging is exclusively based on isotropic density.

Initialization In contrast to R^2 -Gaussian splatting¹⁸, which initializes kernels with the Feldkamp-Davis-Kress (FDK) algorithm⁵³, our IXGS approach requires random initialization due to the non-circular and arbitrary acquisition poses used in our pipeline, where FDK is not applicable. For the evaluations presented in this work, where ground truth CT data was available, the center and dimensions of the reconstruction volume were defined based on the CT. For future clinical applications, the volume origin/dimensions would need to be estimated directly from the calibrated input views, for instance, using techniques like the linear triangulation of principal image axes demonstrated in our prior work¹⁷. Initial kernel positions \mathbf{p}_i were then randomly sampled within this volume. Initial densities ρ_i are uniformly sampled, and the covariances Σ_i are initialized as isotropic matrices with predefined scale values.

Projection and Rendering We refine the 3D Gaussian kernels \mathbb{G}^3 by matching their rendered projections against a set of N input 2D images $\{\mathbf{I}^i\}_{i=1 \dots N}$ (representing \mathbf{I}_{ST} , \mathbf{I}_{real} , or \mathbf{I}_{DRR} depending on the experiment) acquired from known camera poses $\{\mathbf{P}^i\}_{i=1 \dots N}$. For each input view i , a corresponding projected image $\mathbf{I}_{\text{proj}}^i$ is generated by rendering the current 3D Gaussians \mathbb{G}^3 using pose \mathbf{P}^i .

Conceptually, the value of a pixel in I_{proj}^i corresponding to a camera ray $\mathbf{r}(t)$ is computed by integrating the densities of all 3D Gaussian kernels G_j^3 along that ray:

$$I_{\text{proj}}^i(\mathbf{r}) = \sum_{j=1}^M \int G_j^3(\mathbf{r}(t)) dt. \quad (7)$$

Here, $G_j^3(\mathbf{r}(t))$ (defined by $\mathbf{p}_j, \Sigma_j, \rho_j$) refers to the density function evaluated along the ray $\mathbf{r}(t)$, which originates from the X-ray source and intersects the image plane at specific pixel coordinates.

To project the Gaussian kernels for X-ray rendering, we first map the 3D Gaussians (G_j^3) from world space to the C-arm space specific to view i using the transformation \mathbf{T}^i (Equation 1). In the C-arm space, the origin is at the X-ray source, and the z-axis points toward the projection center.

Since a C-arm with its cone-beam X-ray scanner can be modeled similarly to a pinhole camera, we follow^{18,54} and further transfer the Gaussians from C-arm space to a ray space. In ray space, the viewing rays are aligned parallel to the third coordinate axis, simplifying the geometry and facilitating analytical integration along the ray's path. Due to the non-Cartesian nature of ray space, a local affine transformation is applied^{18,54}. In this step, the Jacobian of the affine approximation is computed from the full projection — which, when linearized at the kernel centers, implicitly incorporates the shot-specific intrinsic parameters — and is used to scale the original Gaussian parameters. This yields view-dependent 3D parameters in ray space: position $\tilde{\mathbf{p}}_j^i$ and covariance $\tilde{\Sigma}_j^i$ for each 3D Gaussian j as observed from view i .

Following the derivation in¹⁸, the integration along the ray-space viewing axis (x_2) results in a sum of 2D Gaussians projected onto the image plane. Let $\hat{\mathbf{x}} \in \mathbb{R}^2$ be the 2D coordinates on the image plane corresponding to ray \mathbf{r} . Let $\hat{\mathbf{p}}_j^i \in \mathbb{R}^2$ and $\hat{\Sigma}_j^i \in \mathbb{R}^{2 \times 2}$ be the 2D position and the covariance obtained by dropping the third row and column from $\tilde{\mathbf{p}}_j^i$ and $\tilde{\Sigma}_j^i$, respectively. To ensure accurate density reconstruction across views, the original 3D density ρ_j is scaled by a view-dependent, covariance-related factor $\mu_j^i = \sqrt{2\pi|\hat{\Sigma}_j^i|/|\hat{\Sigma}_j^i|}$, yielding the effective 2D density $\hat{\rho}_j^i = \mu_j^i \rho_j$. This scaling corrects the integration bias inherent in standard Gaussian splatting projections, as detailed in¹⁸. The final rendered intensity at pixel $\hat{\mathbf{x}}$ is then computed by summing these projected 2D Gaussian contributions:

$$I_{\text{proj}}^i(\hat{\mathbf{x}}) \approx \sum_{j=1}^M G_j^2(\hat{\mathbf{x}} | \hat{\rho}_j^i, \hat{\mathbf{p}}_j^i, \hat{\Sigma}_j^i), \quad (8)$$

where G_j^2 represents the contribution of the j -th Gaussian projected onto the 2D image plane, parameterized by its effective 2D density $\hat{\rho}_j^i$, position $\hat{\mathbf{p}}_j^i$, and covariance $\hat{\Sigma}_j^i$. Unlike the original R^2 -Gaussian work, which focused on circular paths, our IXGS approach implements this projection for arbitrary poses $\{\mathbf{P}^i\}_{i=1..N}$. The resulting rendered projections $\{I_{\text{proj}}^i\}_{i=1..N}$ provide the basis for optimizing the 3D scene representation.

Optimization The optimize the 3D Gaussian kernels (\mathbb{G}^3) we minimize a loss function calculated by comparing each rendered projection I_{proj}^i to its corresponding input image \mathbf{I}^i and summing the loss across all N views. The loss combines an L1 difference, the structural similarity index measure (SSIM)⁵⁵, and total variation⁵⁶. The derived gradients of this total loss are then backpropagated to adjust the Gaussian parameters ($\mathbf{p}_j, \Sigma_j, \rho_j$). This optimization, in combination with adaptive density control mechanisms adopted from^{18,30}, iteratively refines the 3D Gaussians (\mathbb{G}^3) until they represent an accurate 3D scene consistent with the input sparse views.

Output For the final 3D reconstruction, the optimized Gaussian kernels \mathbb{G}^3 are converted into a volumetric density map \mathbf{V} using the differentiable voxelizer operator \mathcal{V} from¹⁸:

$$\mathbf{V} = \mathcal{V}(\mathbb{G}^3) \quad (9)$$

This operator partitions the target space into discrete 3D tiles and aggregates kernel contributions within each tile.

Using Equation 9, we generate volumes (denoted \mathbf{V}_{ST} or \mathbf{V}_{real} depending on the input image type) which predominantly capture bony structures, alongside some soft tissue and occasional artifacts inherent to the splatting process. To suppress artifacts and isolate the region of interest (e.g., the lumbar spine), postprocessing involving a thresholding step (empirically set to the 80th percentile) and cropping is applied.

These processed volumes (\mathbf{V}) are the primary 3D output used for qualitative evaluation. They can be visualized directly using 3D rendering techniques. To further enhance inspection of the 3D volume, interactive clipping planes, oriented parallel to

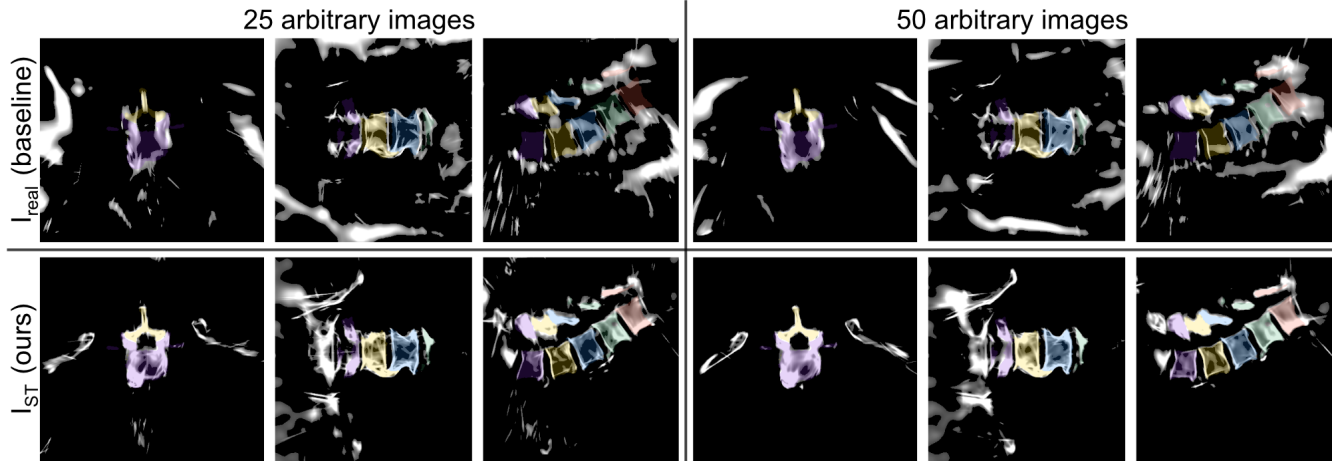


Figure 3. Comparison of 3D reconstructions of the lumbar spine (axial, coronal, and sagittal slices). Each block shows axial, coronal, and sagittal slices of the reconstructed volume, overlaid with alpha-blended masks of the segmented lumbar spine from the ground truth CT for better accuracy assessment. The columns compare reconstructions using 25 views (left) and 50 views (right). The top row shows reconstructions from I_{real} baseline, while the bottom row displays reconstructions from I_{ST} (our approach).

the volume faces, were implemented. These movable planes allow users to cut through the volume and reveal internal structures. Alternatively, the volumes can be inspected via standard clinical multiplanar slices (axial, coronal, and sagittal).

Additionally, for quantitative benchmarking purposes, 2D projections I_{proj} were generated by rendering the optimized 3D Gaussians (\mathbb{G}^3) from the poses corresponding to the held-out test set images (using Equation 8).

Experiments and Performance Evaluation

The performance evaluation assessed the reconstructed 3D volumes and the quality of novel synthesized 2D views. The 3D evaluation focused on a qualitative assessment of clinical usability performed by an expert surgeon. The 2D evaluation used standard quantitative metrics (peak signal-to-noise ratio (PSNR), SSIM) calculated by comparing synthesized views against held-out test images, for benchmarking against prior work.

3D Evaluation An experienced orthopedic surgeon reviewed the 3D reconstructions to rate their anatomical accuracy and usability for intraoperative navigation tasks, specifically focusing on pedicle screw placement. The evaluation centered on clearly depicting key lumbar spine landmarks, including the pedicles, spinous processes, and vertebral endplates. Ratings were provided using the following 4-point Likert scale:

- 4: **Very good** — Clear anatomy and reliable orientation; suitable for navigation.
- 3: **Acceptable** — All major landmarks discernible; acceptable for navigation.
- 2: **Poor** — Only some major landmarks discernible, potentially limiting utility for navigation.
- 1: **Unusable** — Anatomical structures indistinguishable; ineffective for navigation.

For each reconstruction, generated using varying numbers of arbitrary I_{ST} images (ranging from 5 to 50 views, in increments of 5), the surgeon evaluated by examining both the direct 3D visualization and the slices (sagittal, coronal, and axial) in two independent sessions. To aid the evaluation, the surgeon utilized an overlay feature displaying the ground truth segmentations for vertebrae L1 to L5 (see Figure 3). This allowed for direct comparison between the reconstructed anatomy slices and the known ground truth, enabling the surgeon to toggle the overlay freely to assess spatial alignment and anatomical completeness.

2D Quantitative Evaluation and Projection Assessment We assessed reconstruction quality quantitatively using the established 2D metrics PSNR and SSIM⁵⁵, comparing rendered views against held-out test images. We evaluated reconstruction based on I_{ST} against reconstructions from I_{DRR} and I_{real} . Each of these configurations was tested using both 50 and 25 input images per specimen. The I_{DRR} images — generated directly from the ground truth CT scans using the exact same arbitrary poses as the corresponding I_{real} images — serve as a synthetic benchmark and represent the target appearance domain for our proposed I_{ST} radiographic standardization step. Second, as a baseline representing idealized conditions, we applied the original

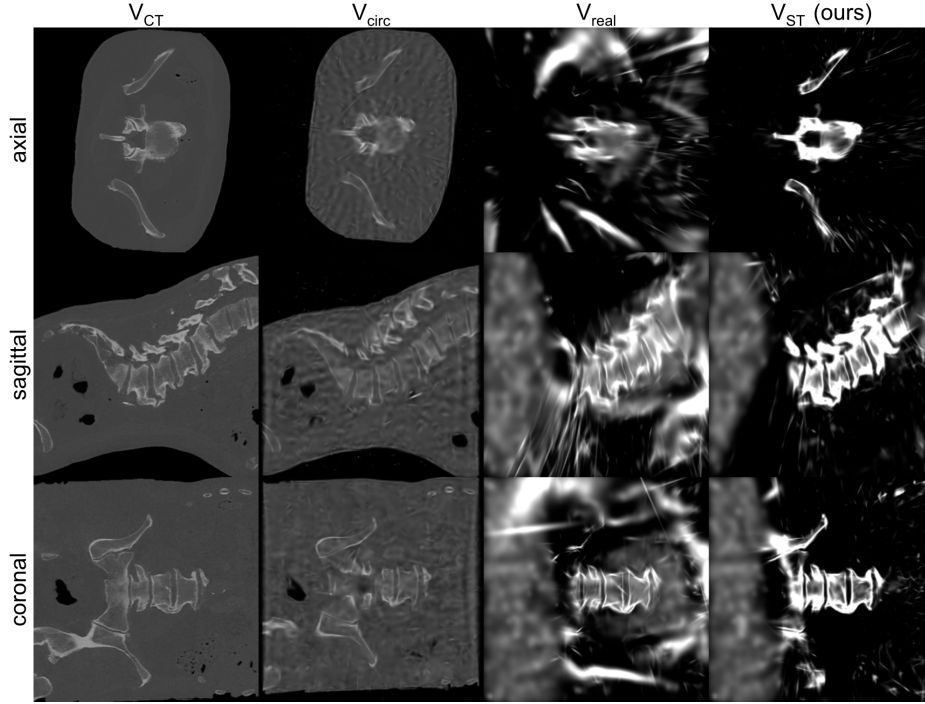


Figure 4. Comparison of slices from reconstructed volumes using different inputs and methods. From left to right: V_{CT} : Ground Truth CT volume, V_{circ} : Reconstruction from 50 synthetic DRRs generated from circular acquisition, V_{real} : Reconstruction from 50 X-rays generated from arbitrary poses, V_{ST} (our approach): Reconstruction from 50 style-transferred X-rays.

R^2 -Gaussian framework¹⁸ to synthetic *ex-vivo* human images generated with circular acquisition paths referred to as (I_{circ}), also using 50 and 25 views per specimen.

To investigate the impact of view count on reconstruction quality, we measured PSNR and SSIM while varying the number of input images for one representative *ex-vivo* specimen. Input views were incrementally increased from 5 to 50 (in steps of 5), and the resulting reconstruction quality was evaluated against the corresponding test set.

We also compared our results against the benchmark performance of the original R^2 -Gaussian framework¹⁸ on real X-rays of the simpler FIPS dataset objects (walnuts, pinecones, seashells), which also utilized circular acquisition paths (using 50 and 25 views).

These quantitative comparative experiments allow us to isolate and assess the effects of different acquisition paths (circular vs. arbitrary) and image types (synthetic, real, style-transferred), thereby evaluating the efficacy of our framework adaptations and the proposed radiographic standardization step (I_{ST}).

Implementation Details

For the implementation of our proposed IXGS framework, we adapted the official implementation of R^2 -Gaussian (https://github.com/Ruyi-Zha/r2_gaussian). Our adapted code will be released at <https://github.com/MrMonk3y/IXGS>.

For the anatomy-guided standardization, we utilized the official PyTorch implementation of Pix2Pix (<https://github.com/junyanz/pytorch-CycleGAN-and-pix2pix>) with default hyperparameters. Due to memory constraints, images were resized to 512×512 pixels before training. The network was trained for 200 epochs, with a batch size of 1. The learning rate was set to 0.0002, and the Adam optimizer was used with $\beta_1 = 0.5$ and $\beta_2 = 0.999$.

The training of the Gaussian splats was conducted on an NVIDIA A100 GPU with 40GB of memory. We followed the default hyperparameters provided by the authors of R^2 Gaussian¹⁸, which produced slightly better results for our target volumes based on empirical evaluation. The network was trained for 30k iterations.

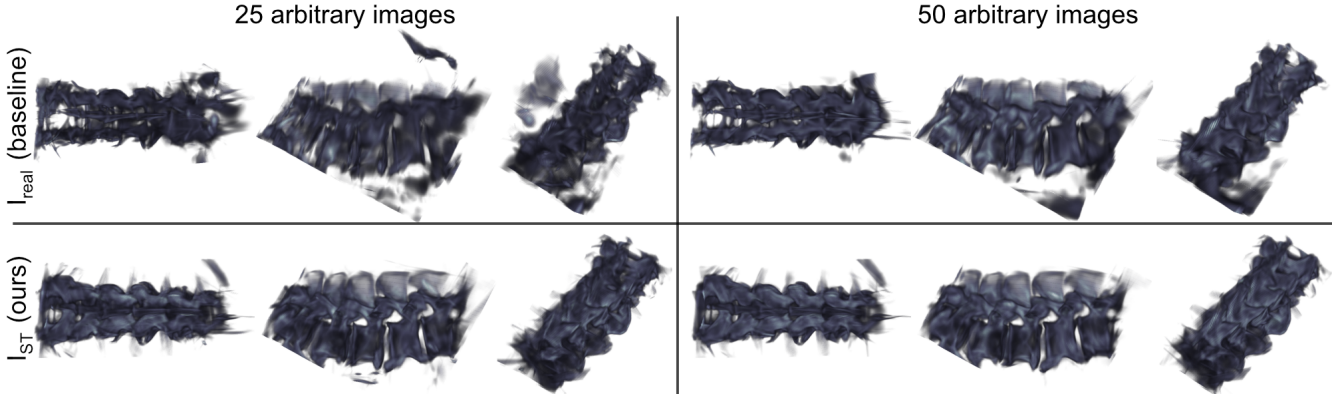


Figure 5. Comparison of 3D reconstructions of the lumbar spine. Each block shows AP, lateral, and isometric views of the reconstructed volume. The columns compare reconstructions using 25 views (left) and 50 views (right). The top row displays reconstructions from I_{real} baseline, while the bottom row shows reconstructions from I_{ST} (our approach).

Results

This section details the performance evaluations conducted in this study. We begin with the qualitative 3D assessment, where an experienced surgeon rated the clinical usability of the reconstructed volumes (Section). Following this, we report the quantitative metrics assessing the 2D reconstruction quality across different input types, acquisition geometries, and view counts, including comparisons to baseline methods (Section).

Figure 4 provides an initial comparison of representative slices, illustrating the core challenges addressed in this work. The reconstruction from a circular acquisition path V_{circ} closely resembles the ground truth CT slices V_{CT} , demonstrating the potential reconstruction quality under idealized conditions. However, the reconstruction using I_{real} shows a notable decrease in quality. Anatomical clarity is reduced, particularly evident in the axial slice, where bone structures are indistinct. In contrast, the reconstruction using I_{ST} shows clear bone structures. A general characteristic visible in all presented Gaussian splat reconstructions is the presence of residual cloudy regions, which correspond to areas not covered by the input views, originating from the random initialization.

Assessment of the 3D Volume Reconstruction Quality

Figures 5 and 3 show representative examples of the volumetric renderings and corresponding slice views, respectively, that were presented independently to the surgeon for evaluation. The surgeon’s usability ratings, aggregated over all six *ex vivo* specimens using 5 to 50 input I_{ST} images (in increments of 5), are summarized in Figure 6a) for volume renderings and Figure 6b) for slice views.

For the direct volume rendering assessment (Figure 6a), ratings were generally ‘Poor’ or ‘Unusable’ when using less than 15 input images. From 20 input images onwards, some specimens achieved ‘Acceptable’ ratings, with ‘Very Good’ ratings appearing at 30 images. Notably, one specimen never surpassed ‘Poor’ ratings regardless of the number of input images used for reconstruction.

A similar trend was observed for the slice view assessment (Figure 6b), although the quality thresholds shifted slightly. The first ‘Acceptable’ ratings for slice visualizations were achieved with 15 input images. However, ratings generally remained lower than those for the corresponding volume renderings up to 45 input images. For one specimen, slice ratings remained ‘Poor’ until 50 input images were used, at which point they reached an ‘Acceptable’ level. At the maximum of 50 input images, the majority of ratings for slice views indicated ‘Very Good’ quality.

Quantitative 2D Reconstruction Quality

Table 1 compares the average PSNR and SSIM across the different reconstruction conditions, evaluated against the test views. Focusing first on the experiments using 50 input images, the baseline condition achieved by applying the original R^2 -Gaussian framework¹⁸ to our synthetic circular dataset I_{circ} , yielded the highest average scores with 39.0 dB PSNR and 0.97 SSIM. When using synthetic but arbitrarily posed I_{DRR} as input to our adapted framework, the performance decreased to 29.45 dB PSNR and 0.89 SSIM. The transition to using 50 arbitrarily posed real X-rays I_{real} resulted in a further decrease, yielding the lowest average PSNR of 23.22 dB and an SSIM of 0.76. Applying our proposed anatomy-guided radiographic standardization I_{ST} improved performance compared to using raw I_{real} inputs, reaching an average PSNR of 25.73 dB (an increase of 2.51 dB) and an SSIM of 0.79, representing a partial recovery towards the I_{DRR} scores.

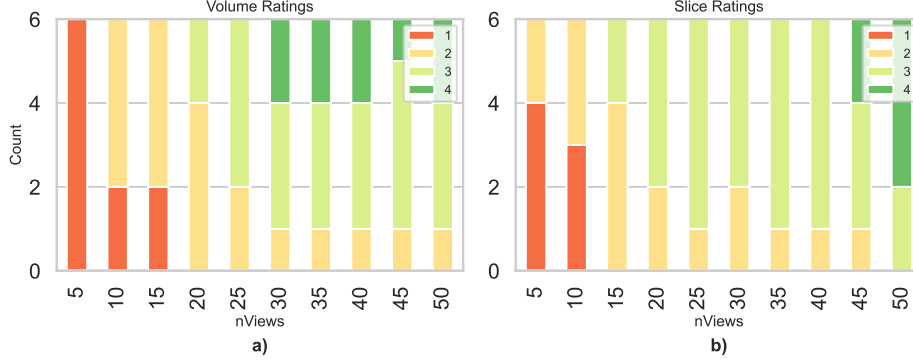


Figure 6. Evaluation of reconstruction quality using Likert ratings from expert surgeons. a) and b) show ratings over 5 to 50 views, with a) assessing 3D volumes and b) assessing slice representations. See Section for details on the different Likert scales used.

Method	50 Views		25 Views	
	PSNR \uparrow	SSIM \uparrow	PSNR \uparrow	SSIM \uparrow
I_{circ}	39.19	0.970	33.51	0.940
I_{DRR}	29.45	0.890	26.62	0.830
I_{real}	23.22	0.760	20.52	0.720
I_{ST} (ours)	25.73	0.790	24.17	0.750

Table 1. Comparison of PSNR and SSIM for different input types. The input types include I_{circ} (a synthetic and circular baseline), I_{DRR} (synthetic DRRs), I_{real} (real X-rays), and I_{ST} (style-transferred, ours). Performance is measured across two view counts: 25 and 50.

The results obtained using 25 input images, also shown in Table 1, followed similar trends but exhibited generally lower metric values across all conditions compared to the 50-image experiments. Notably, the relative improvement in PSNR when using I_{ST} compared to I_{real} was more pronounced than the corresponding improvement in SSIM for both 50-view and 25-view cases.

Figure 7 shows the PSNR/SSIM performance over a varying number of input I_{ST} views from 5 to 50 for one *ex-vivo* specimen. The lowest average performance was observed with only five input images, yielding 17.5 dB PSNR and 0.53 SSIM. Both metrics showed a substantial increase up to 20 input images. Beyond 20 images, the rate of improvement decreased, with performance gradually reaching a maximum average of 25.7 dB PSNR and 0.79 SSIM at 50 input images. This quantitative trend, particularly the sharp initial improvement and later plateauing, can be compared with the qualitative usability assessments presented in Section .

The original R^2 -Gaussian paper¹⁸ reported performance for reconstructions from synthetic circular data, averaged over various objects, including two human torso CTs. They achieved average PSNR and SSIM values of 37.98 dB and 0.952, respectively, using 50 input images, and 35.19 dB and 0.923, respectively, using 25 images. These results align well with our own baseline experiment using purely *ex-vivo* synthetic circular data (I_{circ}), where we achieved slightly higher values (39.0 dB / 0.97 for 50 images). For their experiments on real, albeit circularly acquired, X-rays from the much simpler FIPS dataset³⁹ consisting of objects like seashells and pine cones, they achieved 38.24 dB PSNR / 0.864 SSIM for 50 images and 34.83 dB PSNR / 0.833 SSIM for 25 images. These scores, obtained under circular acquisition of simpler objects, are notably higher than those we obtained for our I_{real} condition, which involved reconstructions from real X-rays with complex anatomy and arbitrary poses.

The average reconstruction time of IXGS using 50 I_{ST} images was 13m 33s on the hardware detailed in Section . For comparison, the original R^2 -Gaussian paper¹⁸ also reported similar timings, such as 13m 52s for 30k training iterations. However, the authors of¹⁸ noted that high-quality results could be achieved much faster under specific conditions, reporting convergence in only 2m 35s on synthetic datasets using just 10k iterations.

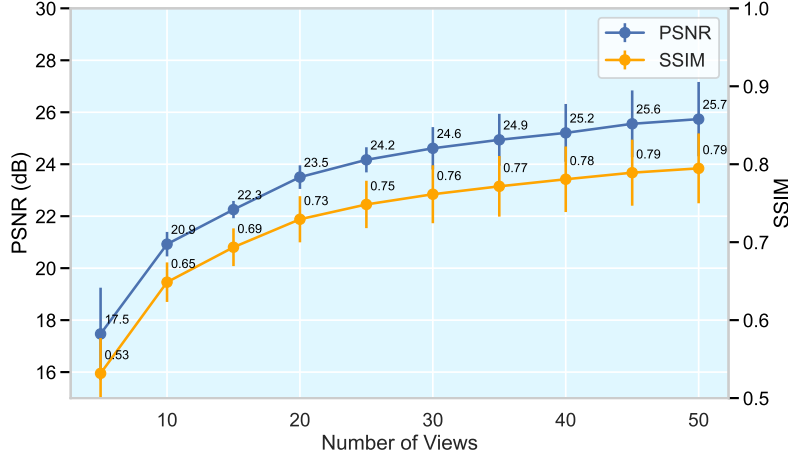


Figure 7. Evaluation of novel view synthesis quality from unseen poses using PSNR and SSIM metrics over varying numbers of views. Higher scores indicate better reconstruction quality.

Discussion

Our IXGS framework demonstrates that 3D volumetric reconstruction from sparse, arbitrarily posed intraoperative X-ray views using Gaussian splatting is feasible, using our proposed pipeline. While state-of-the-art methods benchmarked on synthetic data or real data from controlled circular trajectories show high fidelity¹⁸, we validated our approach in a clinically relevant setting using real *ex-vivo* data with sparse, arbitrary views mimicking intraoperative conditions. Crucially, our results indicate that clinically acceptable reconstructions (‘Acceptable’ to ‘Very Good’ surgeon ratings) can be achieved, particularly when approximately 20-30 or more views are available (Section), marking an important step towards practical surgical navigation applications.

Our quantitative results (Section) confirm a performance gap compared to idealized benchmarks. Reconstructions from arbitrary real X-rays (\mathbf{I}_{real} , \mathbf{I}_{ST}) yield lower PSNR/SSIM scores than those from synthetic circular (\mathbf{I}_{circ}) or even synthetic arbitrary (\mathbf{I}_{DRR}) data. Furthermore, early experiments indicated that simply increasing the number of Gaussians or tuning hyperparameters — while potentially offering minor improvements for real data — was insufficient to match the fidelity achieved with synthetic inputs and quickly became computationally infeasible. This highlights the combined difficulty posed by the domain gap (real vs. synthetic) and complex, arbitrary acquisition geometry. For instance, using 50 views, our \mathbf{I}_{ST} reconstructions achieved an average PSNR of 25.73 dB, substantially lower than the 39.0 dB for \mathbf{I}_{circ} but representing a necessary trade-off for clinical applicability.

Despite modest quantitative scores (PSNR/SSIM), expert evaluation consistently indicated that the reconstructions, especially using \mathbf{I}_{ST} , provide anatomically useful representations for navigation (Section). This highlights the known limitations of standard metrics like PSNR and SSIM, which often correlate poorly with anatomical plausibility, diagnostic quality, or task-specific utility in complex medical image reconstruction scenarios^{57,58}. The ongoing development of learned perceptual metrics, such as LPIPS⁵⁹, indicates efforts to align evaluation with human visual assessment better. However, clinical task performance may require even more specific validation. Our observations reflect this gap: perceived reconstruction quality frequently improved beyond the saturation point of PSNR/SSIM during training or with added views. This supports the necessity of including qualitative, task-based assessments, like expert ratings, when evaluating clinical potential.

The 3D evaluation further highlights the benefits of the proposed style transfer step (\mathbf{I}_{ST}). Notably, reconstructions generated directly from the original \mathbf{I}_{real} images were found to be of insufficient quality for clinical usability assessment and were thus excluded from the expert rating process. This underscores the effectiveness of the \mathbf{I}_{ST} approach, which improved the visibility of bone margins and overall anatomical clarity, leading to higher usability ratings (implicit from Fig. 4, quantitative gain in Section , qualitative benefit in Section). This confirms that \mathbf{I}_{ST} acts as an effective anatomy-guided radiographic standardization, improving consistency across views acquired under varying conditions and mitigating challenges from the domain gap and arbitrary geometry.

Compared to previous work¹⁷, the proposed IXGS approach requires no anatomy-specific pretraining, enhancing its adaptability to new patients, pathologies, or anatomies. However, this flexibility comes at the cost of requiring more input views (~ 20 -30 for usability vs. 4 for X23D) and reconstruction time (13m 33s reported, Section). While this time is significantly longer than the near-instantaneous inference (81.1ms) of a pre-trained model like our previous work X23D¹⁷, convergence might potentially be accelerated using strategies like coarse initialization¹⁸. Furthermore, the scalability to larger fields of view

or higher resolutions without retraining remains an advantage over fixed-resolution methods.

From a clinical perspective, achieving usable 3D volumes intraoperatively from sparse, arbitrary X-rays is highly relevant. The surgeon's feedback during the qualitative assessment provided noteworthy insights. Specifically, it was observed that the generated slice views were oriented parallel to the axes of the reconstruction volume itself, rather than necessarily representing true anatomical planes aligned perfectly with the patient's anatomy. This distinction was reportedly most noticeable in the axial views (e.g., Figure 3) and may have influenced usability ratings. Despite this observation about alignment, the surgeon also noted a general preference for the slice-based visualization over direct volume rendering, stating that scrolling through slices allowed for better spatial perception of anatomical relationships critical for navigation planning. This suggests that interactive slice viewers, potentially enhanced with improved anatomical alignment or artifact reduction, are a promising interface for navigation based on these reconstructions. The 'cloudy' artifacts observed outside the viewed regions (Fig. 4), stemming from the Gaussian splatting initialization in unconstrained areas, are a limitation needing consideration, though often outside the primary surgical volume. Simple postprocessing or focusing on slice views can mitigate their impact.

Current limitations include the reconstruction time (though potentially addressable with initialization strategies), the demonstrated dependency on view count and quality, characteristic reconstruction artifacts (e.g., 'cloudy' regions) in sparsely viewed areas, and visualization nuances such as volume-axis-aligned slices, which require consideration in downstream applications.

Based on these findings, several future research directions emerge. Addressing robustness, particularly regarding challenging input views or outlier cases (like the poorly performing specimen in Section), is crucial. Improving visualization by mitigating artifacts or enabling anatomically aligned slicing requires investigation. Developing evaluation metrics that are better correlated with clinical utility remains an open challenge. Continued exploration of calibration-free workflows, coarse-to-fine reconstruction strategies for speed, and real-time updates integrated into navigation systems are promising avenues.

Conclusions

We adapted Gaussian splatting within our proposed IXGS framework for 3D volumetric reconstruction from sparse (~20-30+ views), arbitrarily posed real intraoperative X-rays, demonstrating feasibility beyond idealized circular or synthetic settings common in prior work. This extends neural rendering techniques toward clinically realistic C-arm imaging scenarios.

Our proposed anatomy-guided radiographic standardization (I_{ST}) using style transfer proved crucial. By reducing input appearance inconsistencies and enhancing relevant bone features, it simplified the reconstruction task for the Gaussian splatting optimization, yielding reconstructions with sufficient anatomical clarity for clinical navigation tasks, as confirmed by expert surgeon assessment.

This clinical usability was achieved despite modest quantitative scores (PSNR/SSIM), highlighting the limitations of standard metrics for capturing task-specific utility. Furthermore, our approach requires no anatomy-specific pretraining, offering significant adaptability advantages over specialized deep learning models for diverse patients and pathologies.

Future work should focus on accelerating reconstruction, improving robustness to challenging inputs and outlier cases, enhancing visualization methods to handle artifacts and potentially provide anatomically aligned slices, developing calibration-free approaches, establishing more clinically relevant evaluation metrics, and ultimately, integrating these techniques into real-time intraoperative navigation systems. This study represents a significant step towards leveraging neural rendering techniques for comprehensive 3D surgical guidance from standard C-arm fluoroscopy.

References

1. Tonetti, J., Boudissa, M., Kerschbaumer, G. & Seurat, O. Role of 3D intraoperative imaging in orthopedic and trauma surgery. *Orthop. & Traumatol. Surg. & Res.* **106**, S19–S25, DOI: [10.1016/j.otsr.2019.05.021](https://doi.org/10.1016/j.otsr.2019.05.021) (2020).
2. Keil, H. *et al.* Intraoperative revision rates due to three-dimensional imaging in orthopedic trauma surgery: results of a case series of 4721 patients. *Eur. J. Trauma Emerg. Surgery: Off. Publ. Eur. Trauma Soc.* **49**, 373–381, DOI: [10.1007/s00068-022-02083-x](https://doi.org/10.1007/s00068-022-02083-x) (2023).
3. Hong, J. & Hashizume, M. An effective point-based registration tool for surgical navigation. *Surg. Endosc.* **24**, 944–948, DOI: [10.1007/s00464-009-0568-2](https://doi.org/10.1007/s00464-009-0568-2) (2010).
4. Ma, Q. *et al.* Autonomous Surgical Robot With Camera-Based Markerless Navigation for Oral and Maxillofacial Surgery. *IEEE/ASME Transactions on Mechatronics* **25**, 1084–1094, DOI: [10.1109/TMECH.2020.2971618](https://doi.org/10.1109/TMECH.2020.2971618) (2020). Conference Name: IEEE/ASME Transactions on Mechatronics.
5. Suenaga, H. *et al.* Vision-based markerless registration using stereo vision and an augmented reality surgical navigation system: a pilot study. *BMC Med. Imaging* **15**, 51, DOI: [10.1186/s12880-015-0089-5](https://doi.org/10.1186/s12880-015-0089-5) (2015).

6. Zheng, J., Miao, S., Wang, Z. J. & Liao, R. Pairwise domain adaptation module for CNN-based 2-D/3-D registration. *J. Med. Imaging (Bellingham, Wash.)* **5**, 021204, DOI: [10.1117/1.JMI.5.2.021204](https://doi.org/10.1117/1.JMI.5.2.021204) (2018).
7. Ferrante, E., Oktay, O., Glocker, B. & Milone, D. H. On the Adaptability of Unsupervised CNN-Based Deformable Image Registration to Unseen Image Domains. In Shi, Y., Suk, H.-I. & Liu, M. (eds.) *Machine Learning in Medical Imaging*, 294–302, DOI: [10.1007/978-3-030-00919-9_34](https://doi.org/10.1007/978-3-030-00919-9_34) (Springer International Publishing, Cham, 2018).
8. Zhang, J. N., Fan, Y. & Hao, D. J. Risk factors for robot-assisted spinal pedicle screw malposition. *Sci. Reports* **9**, 3025, DOI: [10.1038/s41598-019-40057-z](https://doi.org/10.1038/s41598-019-40057-z) (2019). Publisher: Nature Publishing Group.
9. Rahmathulla, G., Nottmeier, E. W., Pirris, S. M., Deen, H. G. & Pichelmann, M. A. Intraoperative image-guided spinal navigation: technical pitfalls and their avoidance. *Neurosurg. Focus.* **36**, E3, DOI: [10.3171/2014.1.FOCUS13516](https://doi.org/10.3171/2014.1.FOCUS13516) (2014).
10. Venkatesh, E. & Elluru, S. V. Cone beam computed tomography: basics and applications in dentistry. *J. Istanbul Univ. Fac. Dent.* **51**, S102–S121, DOI: [10.17096/jiufd.00289](https://doi.org/10.17096/jiufd.00289) (2017).
11. Costa, F. *et al.* Spinal Navigation: Standard Preoperative: Versus: Intraoperative Computed Tomography Data Set Acquisition for Computer-Guidance System: Radiological and Clinical Study in 100 Consecutive Patients. *Spine* **36**, 2094–2098, DOI: [10.1097/BRS.0b013e318201129d](https://doi.org/10.1097/BRS.0b013e318201129d) (2011).
12. Mendelsohn, D. *et al.* Patient and surgeon radiation exposure during spinal instrumentation using intraoperative computed tomography-based navigation. *The Spine J.* **16**, 343–354, DOI: [10.1016/j.spinee.2015.11.020](https://doi.org/10.1016/j.spinee.2015.11.020) (2016).
13. Villard, J. *et al.* Radiation Exposure to the Surgeon and the Patient During Posterior Lumbar Spinal Instrumentation: A Prospective Randomized Comparison of Navigated Versus Non-navigated Freehand Techniques. *Spine* **39**, 1004, DOI: [10.1097/BRS.0000000000000351](https://doi.org/10.1097/BRS.0000000000000351) (2014).
14. Dea, N. *et al.* Economic evaluation comparing intraoperative cone beam CT-based navigation and conventional fluoroscopy for the placement of spinal pedicle screws: a patient-level data cost-effectiveness analysis. *The Spine J.* **16**, 23–31, DOI: [10.1016/j.spinee.2015.09.062](https://doi.org/10.1016/j.spinee.2015.09.062) (2016).
15. Beck, M., Mittlmeier, T., Gierer, P., Harms, C. & Gradl, G. Benefit and accuracy of intraoperative 3D-imaging after pedicle screw placement: a prospective study in stabilizing thoracolumbar fractures. *Eur. Spine J.* **18**, 1469–1477, DOI: [10.1007/s00586-009-1050-5](https://doi.org/10.1007/s00586-009-1050-5) (2009).
16. Jecklin, S., Jancik, C., Farshad, M., Fürnstahl, P. & Esfandiari, H. X23D—intraoperative 3D lumbar spine shape reconstruction based on sparse multi-view X-ray data. *J. Imaging* **8**, 271, DOI: [10.3390/jimaging8100271](https://doi.org/10.3390/jimaging8100271) (2022). Publisher: MDPI.
17. Jecklin, S. *et al.* Domain adaptation strategies for 3D reconstruction of the lumbar spine using real fluoroscopy data. *Med. Image Analysis* **98**, 103322, DOI: [10.1016/j.media.2024.103322](https://doi.org/10.1016/j.media.2024.103322) (2024). Publisher: Elsevier.
18. Zha, R. *et al.* R^S-Gaussian: Rectifying Radiative Gaussian Splatting for Tomographic Reconstruction. *Adv. Neural Inf. Process. Syst.* **37**, 44907–44934 (2024).
19. Zha, R., Zhang, Y. & Li, H. NAF: Neural Attenuation Fields for Sparse-View CBCT Reconstruction. In Wang, L., Dou, Q., Fletcher, P. T., Speidel, S. & Li, S. (eds.) *Medical Image Computing and Computer Assisted Intervention – MICCAI 2022*, 442–452, DOI: [10.1007/978-3-031-16446-0_42](https://doi.org/10.1007/978-3-031-16446-0_42) (Springer Nature Switzerland, Cham, 2022).
20. Rückert, D., Wang, Y., Li, R., Idoughi, R. & Heidrich, W. NeAT: neural adaptive tomography. *ACM Trans. Graph.* **41**, 55:1–55:13, DOI: [10.1145/3528223.3530121](https://doi.org/10.1145/3528223.3530121) (2022).
21. Rangelov, D., Waanders, S., Waanders, K., van Keulen, M. & Miltchev, R. Impact of Camera Settings on 3D Reconstruction Quality: Insights from NeRF and Gaussian Splatting. *Sensors (Basel, Switzerland)* **24**, 7594, DOI: [10.3390/s24237594](https://doi.org/10.3390/s24237594) (2024).
22. Ye, S., Dong, Z., Hu, Y., Wen, Y. & Liu, Y. Gaussian in the Dark: Real-Time View Synthesis From Inconsistent Dark Images Using Gaussian Splatting. *Comput. Graph. Forum* **43**, e15213, DOI: [10.1111/cgf.15213](https://doi.org/10.1111/cgf.15213) (2024). _eprint: <https://onlinelibrary.wiley.com/doi/pdf/10.1111/cgf.15213>.
23. Isola, P., Zhu, J.-Y., Zhou, T. & Efros, A. A. Image-to-Image Translation with Conditional Adversarial Networks, DOI: [10.48550/arXiv.1611.07004](https://doi.org/10.48550/arXiv.1611.07004) (2018). ArXiv:1611.07004 [cs].
24. Kasten, Y., Doktofsky, D. & Kovler, I. End-To-End Convolutional Neural Network for 3D Reconstruction of Knee Bones from Bi-planar X-Ray Images. In Deeba, F., Johnson, P., Würfl, T. & Ye, J. C. (eds.) *Machine Learning for Medical Image Reconstruction*, 123–133, DOI: [10.1007/978-3-030-61598-7_12](https://doi.org/10.1007/978-3-030-61598-7_12) (Springer International Publishing, Cham, 2020).
25. Shiode, R. *et al.* 2D–3D reconstruction of distal forearm bone from actual X-ray images of the wrist using convolutional neural networks. *Sci. Reports* **11**, 15249, DOI: [10.1038/s41598-021-94634-2](https://doi.org/10.1038/s41598-021-94634-2) (2021). Publisher: Nature Publishing Group.

26. Ge, R. *et al.* X-CTRSNet: 3D cervical vertebra CT reconstruction and segmentation directly from 2D X-ray images. *Knowledge-Based Syst.* **236**, 107680, DOI: [10.1016/j.knsys.2021.107680](https://doi.org/10.1016/j.knsys.2021.107680) (2022).
27. Kar, A., Häne, C. & Malik, J. Learning a Multi-View Stereo Machine. *arXiv:1708.05375 [cs]* (2017).
28. Luchmann, D. *et al.* Spinal navigation with AI-driven 3D-reconstruction of fluoroscopy images: an ex-vivo feasibility study. *BMC Musculoskelet. Disord.* **25**, 925, DOI: [10.1186/s12891-024-08052-2](https://doi.org/10.1186/s12891-024-08052-2) (2024). Publisher: BioMed Central London.
29. Mildenhall, B. *et al.* NeRF: representing scenes as neural radiance fields for view synthesis. *Commun. ACM* **65**, 99–106, DOI: [10.1145/3503250](https://doi.org/10.1145/3503250) (2021).
30. Kerbl, B., Kopanas, G., Leimkuehler, T. & Drettakis, G. 3D Gaussian Splatting for Real-Time Radiance Field Rendering. *ACM Trans. Graph.* **42**, 139:1–139:14, DOI: [10.1145/3592433](https://doi.org/10.1145/3592433) (2023).
31. Rakotosaona, M.-J. *et al.* NeRFMeshing: Distilling Neural Radiance Fields into Geometrically-Accurate 3D Meshes. In *2024 International Conference on 3D Vision (3DV)*, 1156–1165, DOI: [10.1109/3DV62453.2024.00093](https://doi.org/10.1109/3DV62453.2024.00093) (2024). ISSN: 2475-7888.
32. Corona-Figueroa, A. *et al.* MedNeRF: Medical Neural Radiance Fields for Reconstructing 3D-aware CT-Projections from a Single X-ray. *2022 44th Annu. Int. Conf. IEEE Eng. Medicine & Biol. Soc. (EMBC)* 3843–3848, DOI: [10.1109/EMBC48229.2022.9871757](https://doi.org/10.1109/EMBC48229.2022.9871757) (2022). Conference Name: 2022 44th Annual International Conference of the IEEE Engineering in Medicine & Biology Society (EMBC) ISBN: 9781728127828 Place: Glasgow, Scotland, United Kingdom Publisher: IEEE.
33. Cai, Y. *et al.* Radiative Gaussian Splatting for Efficient X-Ray Novel View Synthesis. In Leonardis, A. *et al.* (eds.) *Computer Vision – ECCV 2024*, 283–299, DOI: [10.1007/978-3-031-73232-4_16](https://doi.org/10.1007/978-3-031-73232-4_16) (Springer Nature Switzerland, Cham, 2025).
34. Gao, Z. *et al.* DDGS-CT: Direction-Disentangled Gaussian Splatting for Realistic Volume Rendering. *Adv. Neural Inf. Process. Syst.* **37**, 39281–39302 (2024).
35. Wysocki, M. *et al.* Ultra-NeRF: Neural Radiance Fields for Ultrasound Imaging. In *Medical Imaging with Deep Learning*, 382–401 (PMLR, 2024). ISSN: 2640-3498.
36. Awojoyogbe, B. O. & Dada, M. O. Neural Radiance Fields (NeRFs) Technique to Render 3D Reconstruction of Magnetic Resonance Images. In Awojoyogbe, B. O. & Dada, M. O. (eds.) *Digital Molecular Magnetic Resonance Imaging*, 247–258, DOI: [10.1007/978-981-97-6370-2_10](https://doi.org/10.1007/978-981-97-6370-2_10) (Springer Nature, Singapore, 2024).
37. Yang, S. *et al.* Deform3DGS: Flexible Deformation for Fast Surgical Scene Reconstruction with Gaussian Splatting. In Linguraru, M. G. *et al.* (eds.) *Medical Image Computing and Computer Assisted Intervention – MICCAI 2024*, 132–142, DOI: [10.1007/978-3-031-72089-5_13](https://doi.org/10.1007/978-3-031-72089-5_13) (Springer Nature Switzerland, Cham, 2024).
38. Cai, Y., Wang, J., Yuille, A., Zhou, Z. & Wang, A. Structure-Aware Sparse-View X-ray 3D Reconstruction. 11174–11183 (2024).
39. X-ray Tomographic Datasets Archives.
40. Chen, Y. *et al.* VertXNet: an ensemble method for vertebral body segmentation and identification from cervical and lumbar spinal X-rays. *Sci. Reports* **14**, 3341, DOI: [10.1038/s41598-023-49923-3](https://doi.org/10.1038/s41598-023-49923-3) (2024). Publisher: Nature Publishing Group.
41. Kim, K. C., Cho, H. C., Jang, T. J., Choi, J. M. & Seo, J. K. Automatic detection and segmentation of lumbar vertebrae from X-ray images for compression fracture evaluation. *Comput. Methods Programs Biomed.* **200**, 105833, DOI: [10.1016/j.cmpb.2020.105833](https://doi.org/10.1016/j.cmpb.2020.105833) (2021).
42. Darcet, T., Oquab, M., Mairal, J. & Bojanowski, P. Vision Transformers Need Registers, DOI: [10.48550/arXiv.2309.16588](https://doi.org/10.48550/arXiv.2309.16588) (2024). ArXiv:2309.16588 [cs].
43. Kirillov, A. *et al.* Segment Anything. 4015–4026 (2023).
44. Wu, J. *et al.* Medical SAM Adapter: Adapting Segment Anything Model for Medical Image Segmentation, DOI: [10.48550/arXiv.2304.12620](https://doi.org/10.48550/arXiv.2304.12620) (2023). ArXiv:2304.12620 [cs].
45. Ehab, W., Huang, L. & Li, Y. UNet and Variants for Medical Image Segmentation. *Int. J. Netw. Dyn. Intell.* 100009–100009, DOI: [10.53941/ijndi.2024.100009](https://doi.org/10.53941/ijndi.2024.100009) (2024).
46. Gupta, S., Lakhotia, S., Rawat, A. & Tallamraju, R. ViTOL: Vision Transformer for Weakly Supervised Object Localization. 4101–4110 (2022).

47. Yookwan, W. *et al.* Coarse X-ray Lumbar Vertebrae Pose Localization and Registration Using Triangulation Correspondence. *Processes* **11**, 61, DOI: [10.3390/pr11010061](https://doi.org/10.3390/pr11010061) (2023). Number: 1 Publisher: Multidisciplinary Digital Publishing Institute.
48. Ye, K., Sun, W., Tao, R. & Zheng, G. A Projective-Geometry-Aware Network for 3D Vertebra Localization in Calibrated Biplanar X-Ray Images. *Sensors* **25**, 1123, DOI: [10.3390/s25041123](https://doi.org/10.3390/s25041123) (2025). Number: 4 Publisher: Multidisciplinary Digital Publishing Institute.
49. Wang, C.-Y., Bochkovskiy, A. & Liao, H.-Y. M. YOLOv7: Trainable Bag-of-Freebies Sets New State-of-the-Art for Real-Time Object Detectors. 7464–7475 (2023).
50. Zhu, J.-Y., Park, T., Isola, P. & Efros, A. A. Unpaired Image-To-Image Translation Using Cycle-Consistent Adversarial Networks. In *2017 IEEE International Conference on Computer Vision (ICCV)*, 2223–2232, DOI: [10.1109/ICCV.2017.244](https://doi.org/10.1109/ICCV.2017.244) (IEEE, Venice, 2017).
51. Duda, R. O. & Hart, P. E. Use of the Hough transformation to detect lines and curves in pictures. *Commun. ACM* **15**, 11–15, DOI: [10.1145/361237.361242](https://doi.org/10.1145/361237.361242) (1972).
52. Abdel-Aziz, Y. I., Karara, H. M. & Hauck, M. Direct Linear Transformation from Comparator Coordinates into Object Space Coordinates in Close-Range Photogrammetry*. *Photogramm. Eng. & Remote. Sens.* **81**, 103–107, DOI: [10.14358/PERS.81.2.103](https://doi.org/10.14358/PERS.81.2.103) (2015).
53. Feldkamp, L. A., Davis, L. C. & Kress, J. W. Practical cone-beam algorithm. *JOSA A* **1**, 612–619, DOI: [10.1364/JOSAA.1.000612](https://doi.org/10.1364/JOSAA.1.000612) (1984). Publisher: Optica Publishing Group.
54. Zwicker, M., Pfister, H., van Baar, J. & Gross, M. EWA splatting. *IEEE Transactions on Vis. Comput. Graph.* **8**, 223–238, DOI: [10.1109/TVCG.2002.1021576](https://doi.org/10.1109/TVCG.2002.1021576) (2002).
55. Wang, Z., Bovik, A., Sheikh, H. & Simoncelli, E. Image quality assessment: from error visibility to structural similarity. *IEEE Transactions on Image Process.* **13**, 600–612, DOI: [10.1109/TIP.2003.819861](https://doi.org/10.1109/TIP.2003.819861) (2004). Conference Name: IEEE Transactions on Image Processing.
56. Rudin, L. I., Osher, S. & Fatemi, E. Nonlinear total variation based noise removal algorithms. *Phys. D: Nonlinear Phenom.* **60**, 259–268, DOI: [10.1016/0167-2789\(92\)90242-F](https://doi.org/10.1016/0167-2789(92)90242-F) (1992).
57. Breger, A. *et al.* A study on the adequacy of common IQA measures for medical images, DOI: [10.48550/arXiv.2405.19224](https://doi.org/10.48550/arXiv.2405.19224) (2024). ArXiv:2405.19224 [eess].
58. Dohmen, M., Klemens, M. A., Baltruschat, I. M., Truong, T. & Lenga, M. Similarity and quality metrics for MR image-to-image translation. *Sci. Reports* **15**, 3853, DOI: [10.1038/s41598-025-87358-0](https://doi.org/10.1038/s41598-025-87358-0) (2025). Publisher: Nature Publishing Group.
59. Zhang, R., Isola, P., Efros, A. A., Shechtman, E. & Wang, O. The Unreasonable Effectiveness of Deep Features as a Perceptual Metric. 586–595 (2018).

Acknowledgements

This work has been supported by the OR-X - a Swiss national research infrastructure for translational surgery and associated funding by the University Hospital Balgrist . We like to thank Tanja Walther for her support during the data capture. Financial support was provided by the Monique Dornonville de la Cour Foundation and an internal Balgrist University Hospital fund.

Author contributions statement

S.J.: Conceptualization, Methodology, Software, Validation, Formal analysis, Investigation, Data Curation, Writing - Original Draft, Visualization. A.M.: Software, Writing - Review & Editing. R.Z.: Software, Methodology, Writing - Review & Editing. L.C.: Software, Validation. C.J.L.: Investigation (Clinical Evaluation), Validation. M.F.: Resources, Funding acquisition. P.F.: Conceptualization, Resources, Writing - Review & Editing, Supervision, Funding acquisition, Project administration. All authors reviewed the manuscript.

Data Availability

The code adapted for this study, along with a small dataset for testing derived from the *ex-vivo* data, will be made available at <https://github.com/MrMonk3y/IXGS>. The primary *ex-vivo* paired dataset (real X-rays, DRRs, calibration data) generated and analysed during the current study is not publicly available due to restrictions relating to pending patent applications but is available from the corresponding author on reasonable request.

Competing Interests

S.J. reports that financial support for his doctoral studies was provided by the Monique Dornonville de la Cour Foundation and an internal Balgrist University Hospital fund. M.F. reports a relationship with X23D AG that includes equity or stocks. P.F. reports a relationship with X23D AG that includes board membership and equity or stocks. P.F. and M.F. have patent #WO2023156608A1 pending to University of Zurich related to prior work. P.F., M.F., and S.J. have patent "A computer-implemented method, device, system and computer program product for processing anatomic imaging data" pending to University of Zurich related to prior work. The remaining authors (A.M., R.Z., L.C., C.J.L.) declare that they have no known competing financial interests or personal relationships that could have appeared to influence the work reported in this paper.